

Tunable itinerant spin dynamics with polar molecules

Jun-Ru Li, Kyle Matsuda, Calder Miller, Annette N. Carroll, William G. Tobias, Jacob S. Higgins,
and Jun Ye

¹JILA, National Institute of Standards and Technology and Department of Physics, University of
Colorado, Boulder, CO 80309.

*Corresponding authors. Emails: junru.li@colorado.edu, ye@jila.colorado.edu

Strongly interacting spins underlie many intriguing phenomena and applications ranging from quantum magnetism and spin transport to precision quantum sensing and quantum information processing¹⁻⁴. An interacting spin system with high controllability is desired in order to understand these complex phenomena. Here, we demonstrate tunable itinerant spin dynamics enabled by dipolar interactions using a gas of potassium-rubidium molecules confined to two-dimensional planes, where the spin-1/2 is encoded in the molecular rotational levels. The dipolar interaction gives rise to a shift of the rotational transition frequency and a collision-limited Ramsey contrast decay that emerges from the coupled spin and motion. Both the Ising and spin exchange interactions are precisely tuned by varying the strength and orientation of an electric field, as well as the internal molecular state. This full tunability enables both static and dynamical control of the spin Hamiltonian, allowing reversal of the coherent spin dynamics. Our work establishes an interacting spin platform that allows for exploration of many-body spin dynamics and spin-motion physics utilizing the strong, tunable dipolar interaction.

Ultracold polar molecules, with (pseudo-)spins encoded in the molecules' internal states, provide a unique platform for investigating many-body spin dynamics with high tunability⁵⁻¹⁰. The effective spin coupling is realized via long-range, anisotropic dipolar interactions mediated by the molecule's electric dipole moment, which is tunable with external electric fields and microwaves. Pioneering proposals^{6-8,10} and experiment⁹ used polar molecules localized in optical lattices to realize lattice-spin models. Even with modest lattice fillings, the strong dipolar interaction allowed the observation of spin-exchange dynamics as oscillatory evolution of the Ramsey fringe contrast⁹. Recently, spin correlations have been directly imaged under a microscope¹¹. The strong tunability of this lattice-spin system enables the realization of a variety of spin Hamiltonians displaying exotic correlations and phase transitions^{7,8,12-14}.

In parallel, molecules loaded in a two-dimensional (2D) layer are allowed to move freely within the plane, and dipolar interactions control the collisional process. For instance, the repulsion from the dipolar interaction greatly enhances elastic collisions while suppressing reactive losses, allowing evaporative cooling to quantum degeneracy¹⁵. The engineered dipolar interactions create a strong repulsive energy barrier that allows control of the molecular reaction with only a small change of the electric field^{16,17} or microwaves^{18,19}. For a system with multiple spatially separated 2D layers, local control of the dipolar interaction across the layers allows regulation of the molecular interactions with high spatial resolution²⁰.

Combining coherent spin interactions and motional physics in a single platform is expected to give rise to rich dynamics. In this article, we report the realization of an itinerant spin system that evolves from a fully controlled spin Hamiltonian to a more complex spin-motion coupled system. Isolated 2D layers of dipolar molecules are addressed by a precisely controlled external electric field (E) to realize both Ising and exchange interactions with high tunability (Fig. 1a). At short evolution times, the system's dynamics are governed by dipolar interactions in the spin degrees of freedom, realizing a many-body spin Hamiltonian that can generate highly entangled spin states²¹. At longer times where collisions mediated by the molecular thermal motion and dipolar interaction manifest, we observe the onset of spin decoherence that is not reversible by engineered echo pulse sequences. Our work establishes a tunable dipolar system where the spin and motional dynamics are coupled by strong dipolar interactions.

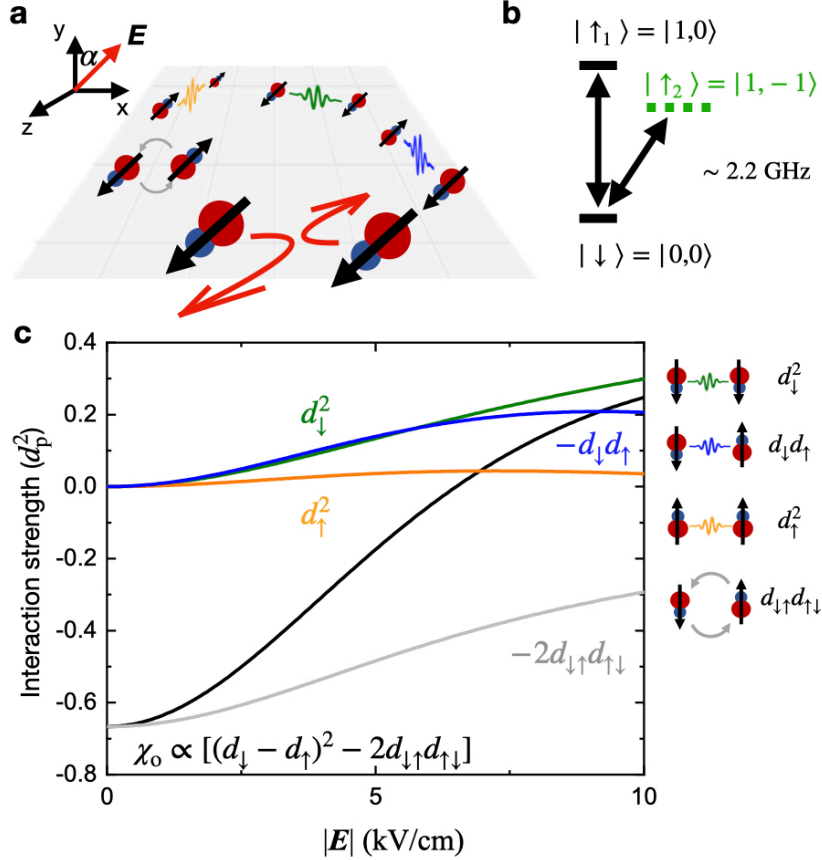


Figure 1. A 2D itinerant spin system with polar molecules. **a.** Molecular spins are free to move within a 2D layer. Their dipolar interactions are tuned by a bias electric field E with configurable magnitude and orientation in the x - y plane. Yellow, blue, green, and grey curves illustrate interaction processes detailed in **c**. Red arrows represent dipolar elastic collisions. **b.** Energy diagram for the ground and first excited rotational states in which we encode the spin-1/2 degree of freedom. The transitions are driven by microwaves. **c.** Calculated dipolar interaction strength as a function of $|E|$ for the spin manifold $\{|\downarrow\rangle, |\uparrow_1\rangle\}$. The dipolar coupling strength is given in units of the permanent dipole moment of KRb $d_p = 0.574$ Debye. The molecules interact via their induced dipole moments d_\downarrow and d_\uparrow , as well as the transition dipole moment $d_{\downarrow\uparrow}$. The black line shows the field dependence of χ_0 .

We create gases of fermionic $^{40}\text{K}^{87}\text{Rb}$ (KRb) loaded into 2D harmonic traps formed by a one-dimensional optical lattice^{15,20} (see Methods). The spin-1/2 degree of freedom is mapped onto molecular rotations as $|\downarrow\rangle = |0, 0\rangle$ and $|\uparrow_1\rangle = |1, 0\rangle$ or $|\uparrow_2\rangle = |1, -1\rangle$ (Fig. 1b). Here, $|N, m_N\rangle$ denotes a rotational state with N being the field-dressed rotational quantum number and m_N its projection on the quantization axis set by E (or the magnetic field along \hat{y} at $|E| = 0$). Spin states are prepared using a microwave field to drive the molecules' rotational transitions. The magnitude and orientation of E and the molecular spin states are used to tune the dipolar interaction, and

consequently, the spin and collision dynamics.

At short times prior to the onset of collisions, the system evolves primarily through the spin-1/2 degree of freedom, as molecular motion is frozen. Dipolar interactions couple individual molecular spins $\mathbf{s}_i = \{s_i^X, s_i^Y, s_i^Z\}$ occupying the harmonic oscillator mode i , leading to spin dynamics described by an XXZ Heisenberg Hamiltonian²¹: $H = \frac{1}{2} \sum_{ij} [J_{ij}^Z s_i^Z s_j^Z + J_{ij}^\perp (s_i^X s_j^X + s_i^Y s_j^Y)] + \sum_i s_i^Z h_i^Z$. Here, h_i^Z is the effective field. J_{ij}^Z and J_{ij}^\perp are the Ising and the exchange interactions arising from the induced dipole moments d_\downarrow and d_\uparrow (originating from \mathbf{E} -induced mixing of the opposite-parity rotational states) and the transition dipole moment $d_{\downarrow\uparrow}$, respectively.

In contrast to lattice spins⁹, spins delocalized in the 2D plane have large and nearly uniform spatial wavefunction overlap between any pairs of molecules. As a result, J_{ij}^\perp , J_{ij}^Z , and h_i^Z have only weak dependence on $\{i, j\}$ and narrowly peak at their ensemble average values J_\perp , J_Z , h_Z , leading to an effective description of dynamics in terms of the collective spin²¹ $S_\gamma = \sum_i s_i^\gamma$ ($\gamma = X, Y, Z$) :

$$H = J_\perp S^2 + \chi_o S_Z^2 + h_Z S_Z . \quad (1)$$

J_\perp enforces an energy cost to change the total spin $|S|$ and thus protects the collective spin from decoherence. h_Z represents an effective magnetic field. The strength of spin-spin interaction is characterized by $\chi_o = J_Z - J_\perp$, which is the difference between the average Ising and exchange interaction. This term produces a one-axis twisting that can generate highly entangled spin states such as spin squeezed states^{21,22} and GHZ states²³. All these terms are tunable with \mathbf{E} or the choice of spin states. In particular, both the magnitude and sign of the interaction parameter $\chi_o \propto (3\cos^2\alpha - 1)[(d_\downarrow - d_\uparrow)^2 - 2d_{\downarrow\uparrow}d_{\uparrow\downarrow}]$ (see Methods) can be varied by changing the angle α between \mathbf{E} and $\hat{\mathbf{y}}$ (Fig. 1a) or $|\mathbf{E}|$, as exemplified by the spin manifold $\{|\downarrow\rangle, |\uparrow_1\rangle\}$ where $d_{\downarrow\uparrow} = d_{\uparrow\downarrow} = \langle\downarrow|d|\uparrow_1\rangle$, depicted in Fig. 1c.

At long times, dipolar interactions lead to molecular collisions. In particular, dipolar elastic collisions change the motional modes of the molecules at a rate depending on the molecular spins and coherence. In the motional degree of freedom, these mode-changing collisions lead to dipolar thermalization¹⁵. In the spin degree of freedom, they cause decoherence of the collective spin at the collision rate because each of the collisional events introduces *random* spin rotations on the two colliding spins. This decoherence cannot be reversed due to scrambled spin-motion coupling.

Our system exhibits unique dynamics arising from the molecular spin and motion intertwined by dipolar interactions: Delocalized molecules facilitate the couplings between molecular spins, and spin dynamics affect the molecular collisions through spin coherence. Using dynamical decoupling techniques, we characterize both effects with Ramsey spectroscopy. The former manifests as a frequency shift on the spin transition, the latter as an interaction dependent fringe contrast decay.

We first characterize the spin dynamics by measuring the frequency shift arising from χ_o , at short times before the onset of collisional decoherence. At the mean-field level, $\chi_o S_Z^2 \approx 2\chi_o S_Z \langle S_Z \rangle$ produces a spin-dependent effective field $2\chi_o \langle S_Z \rangle$ that shifts the spin transition frequency. The magnitude of this shift is proportional to the expectation value of the z-projection of the collective spin $\langle S_Z \rangle$, realized as a coherent superposition of the two spin states with a population imbalance of $(N_\uparrow - N_\downarrow)/2$. Here, N_\uparrow and N_\downarrow are the numbers of molecules in each spin states, with a total number $N_{\text{tot}} = N_\uparrow + N_\downarrow$. For a Ramsey experiment with an interrogation time T and an initial pulse area θ that prepares the system with $\langle S_Z \rangle = -(N_{\text{tot}}/2) \cos\theta$, this leads to a dipolar interaction-induced fringe phase shift

$$\Delta\phi/2\pi = -n\chi T \cos\theta. \quad (2)$$

Here, we introduce a density independent $\chi = (\chi_o/h)(N_{\text{tot}}/n)$, where n is the average 2D molecular density and h is the Planck constant. The strength of the mean-field interaction U_χ is thus defined as $U_\chi = n\chi$.

For a typical density $n = 1 \times 10^7 \text{ cm}^{-2}$, the frequency shift ($\Delta\phi/2\pi T$) is expected to be about 100 Hz. Measuring such shifts requires an appropriately long spin coherence time. Despite the long intrinsic coherence time T_2 between the molecular rotations, the experimentally achieved coherence time T_2^* is limited by single particle dephasing mechanisms^{20,24}. Grey circles in Fig. 2b show decay of the Ramsey contrast for $|\mathbf{E}| = 0$ under typical trapping conditions. A Gaussian fit gives a coherence time T_2^* of only 0.24(1) ms, which is consistent with the coherence being limited by the differential ac polarizability of the two spin states in the optical lattice^{20,24}. Extending T_2^* to milliseconds has been demonstrated by orienting the bias electric field to the *magic angle*^{20,24-26}, with $\alpha \approx 36^\circ$ for our configuration. However, achieving long T_2^* in an arbitrary configuration of \mathbf{E} , which is required for tuning of the dipolar interaction, has been challenging.

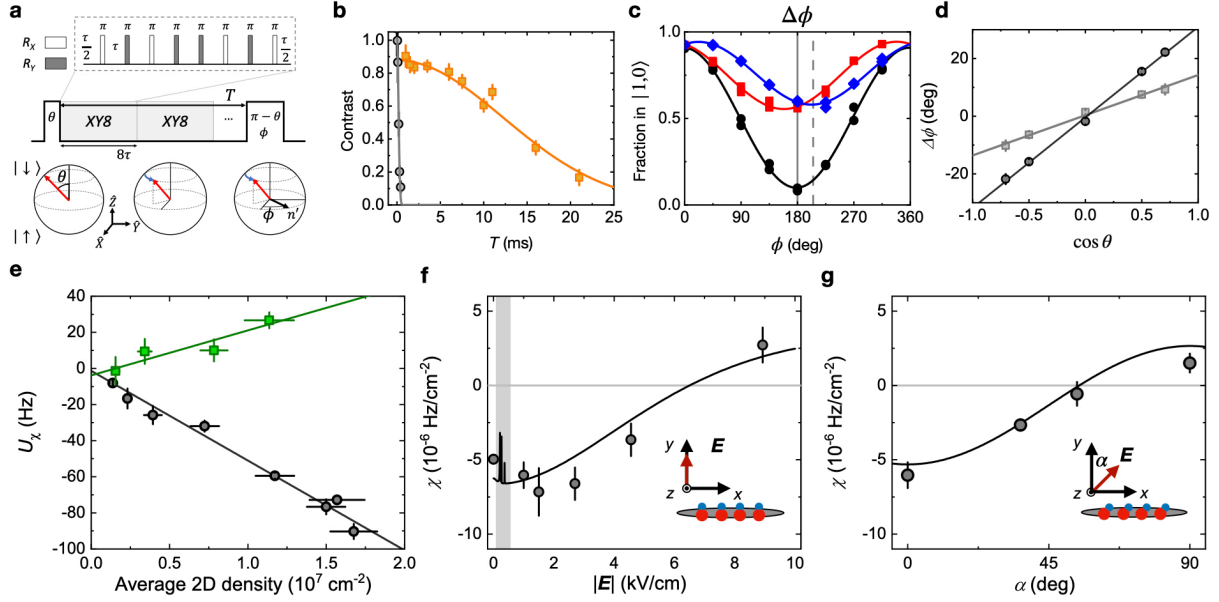


Figure 2. Dynamical decoupling and tunable dipolar interactions between molecules. **a.** The standard Ramsey sequence consists of an initial pulse of area θ , followed by an evolution time T , and finally a pulse of area $\pi - \theta$ about an axis $\hat{n} = \hat{X}\cos\phi + \hat{Y}\sin\phi$. We insert one or more XY8 sequences during T , denoted as XY8 \times M . One XY8 sequence (zoomed region) consists of 8 Rabi- π pulses spaced by time τ , for a total free precession time of 8τ (see Methods). **b.** Decay of Ramsey fringe contrast between $|\downarrow\rangle$ and $|\uparrow_1\rangle$ without dynamical decoupling (grey circles) and with XY8 \times 3 at a density of $n = 0.14(2) \times 10^7 \text{ cm}^{-2}$ (orange squares). **c.** Measured Ramsey fringes with dynamical decoupling for an average 2D density $n = 1.4(1) \times 10^7 \text{ cm}^{-2}$ for initial population imbalance $\theta = \pi/4$ (blue diamonds), $\pi/2$ (black circles) and $3\pi/4$ (red squares) for $T = 1.2 \text{ ms}$ at $|\mathbf{E}| = 0$. Solid lines are fits to $A\cos[(\pi/180)\phi - \Delta\phi]$ plus an offset, from which we extract the measured shift $\Delta\phi$. **d.** Measured $\Delta\phi$ versus $\cos\theta$ for $n = 1.4(1) \times 10^7 \text{ cm}^{-2}$ (black circles) and $0.65(7) \times 10^7 \text{ cm}^{-2}$ (grey squares). The strength of the mean-field interaction U_χ is extracted from the slope of the linear fit (solid lines). **e.** Density dependence of U_χ for the $\{|\downarrow\rangle, |\uparrow_1\rangle\}$ manifold (grey) and the $\{|\downarrow\rangle, |\uparrow_2\rangle\}$ manifold (green). Black and green solid lines are linear fits to the data. The slopes of the fits are direct measurements of χ_1 and χ_2 respectively. **f.** Dependence of χ for the $\{|\downarrow\rangle, |\uparrow_1\rangle\}$ manifold on $|\mathbf{E}|$ at $\alpha = 0^\circ$. The solid line is a one parameter fit to $A[(d_\downarrow - d_\uparrow)^2 - 2d_{\downarrow\uparrow}d_{\uparrow\downarrow}]$ calculated for KRB at the experimental magnetic field and trapping conditions. Shaded area: $|\mathbf{E}| < 500 \text{ V/cm}$ where hyperfine states are strongly mixed. Grey line indicates zero. **g.** Angular dependence of χ for the $\{|\downarrow\rangle, |\uparrow_1\rangle\}$ manifold at $|\mathbf{E}| = 1.02 \text{ kV/cm}$. Solid line is a one parameter fit to $-A(3\cos^2\alpha - 1)$. Grey line indicates zero.

We perform dynamical decoupling with an XY8 multi-pulse sequence²⁷ to suppress single particle dephasing. Similar techniques have been used in NMR²⁸ and NV centers²⁹ to extend T_2^* towards T_2 . An XY8 sequence consists of 8 Rabi- π rotations along \hat{X} and \hat{Y} (Fig. 2a). The consecutive spin

echo pulses spaced by time τ form a bandpass filter³⁰ that rejects noise outside of a window with center frequency $f_0 = 1/(2\tau)$ and width $\sim 1/T$, suppressing the Ramsey phase fluctuations caused by noise in \mathbf{E} and the nonzero differential ac polarizability (see Methods). The XY8 sequence's time-reversal symmetry and alternation between rotation axes further improve robustness against pulse area error and finite pulse duration³¹. Multiple XY8 sequences can be concatenated (denoted XY8 $\times M$) to achieve longer Ramsey time T without affecting f_0 . Implementing XY8 $\times 3$ leads to a factor of 71(5) improvement in T_2^* from 0.24(1) ms to 17(1) ms for the same field and trapping condition (orange squares in Fig. 2b). The measurement is performed at a low $n = 0.14(2) \times 10^7$ cm⁻² to reduce interaction effects. The achieved coherence time is sufficient for studying the dipolar density shift as a function of $|\mathbf{E}|$ and α .

We measure the frequency shift and thus χ with the following procedure: A microwave pulse with an area θ prepares KRB in a superposition state $\cos(\theta/2)|\downarrow\rangle + \sin(\theta/2)|\uparrow_1\rangle$. After a sequence of XY8 with $T = 1.2$ ms (Fig. 2a), the accumulated phase is mapped onto population by a second Ramsey pulse with an area of $\pi - \theta$ and a variable phase ϕ . Molecules in both $|\downarrow\rangle$ and $|\uparrow_1\rangle$ are subsequently imaged²⁰ to obtain the fraction in $|\uparrow_1\rangle$ as a function of ϕ , from which we obtain Ramsey fringes like those shown in Fig. 2c for $|\mathbf{E}| = 0$. By fitting the obtained fringes to a sinusoidal function, we extract the corresponding phase shifts $\Delta\phi$.

At a fixed n , we measure Ramsey fringes at several different values of θ to vary the phase shift. We observe a linear dependence of $\Delta\phi$ on $\cos\theta$ (Fig. 2d). We obtain U_χ as the slope of the linear fit to $\Delta\phi$ versus $\cos\theta$ (solid black and solid grey lines in Fig. 2d).

We repeat the measurement of U_χ at several values of n to measure χ . The results for $|\mathbf{E}| = 0$ are shown with grey circles in Fig. 2e. The measured U_χ as a function of n is well captured by a linear fit, consistent with the mean-field model. From the slope of the fit, we extract $\chi_1 = -4.9(3) \times 10^{-6}$ Hz/cm⁻² at $|\mathbf{E}| = 0$ between $|\downarrow\rangle$ and $|\uparrow_1\rangle$.

Leveraging a configurable $|\mathbf{E}|$ that mixes the molecular rotational states allows us to vary the relative strength between the Ising and exchange interactions in the spin dynamics. We demonstrate this tunability by measuring χ over a wide range of $|\mathbf{E}|$ at $\alpha = 0^\circ$ with the same procedure described above for the manifold $\{|\downarrow\rangle, |\uparrow_1\rangle\}$. The results, shown in Fig. 2f, are well

captured by scaling $\chi \propto [(d_{\downarrow} - d_{\uparrow})^2 - 2d_{\downarrow\uparrow}d_{\uparrow\downarrow}]$ (black solid line) to fit the experimental data. The fit includes modifications to the dipole moments from the mixing of hyperfine and rotational states at $|\mathbf{E}|$ below ~ 500 V/cm. At low $|\mathbf{E}|$, dipolar exchange dominates and $\chi < 0$. As $|\mathbf{E}|$ increases, the increasing strength of the Ising interactions from the induced dipoles competes with the spin exchange eventually leading to $\chi > 0$ (Fig. 1e) at high $|\mathbf{E}|$. Tuning $|\mathbf{E}|$ to approximately 7 kV/cm where $\chi = 0$ would realize the Heisenberg XXX model. In future studies, such tunability will allow exploration of qualitatively different spin dynamics hosted by a spin-1/2 system⁸.

In 2D, the average dipolar interaction can be controlled by orienting the dipole moments relative to the 2D plane, as a direct consequence of the anisotropy of the dipolar interaction. This feature has previously been used to control the dipolar collisional loss between molecules¹⁶. Here, we measure χ between $|\downarrow\rangle$ and $|\uparrow_1\rangle$ as a function of α at fixed $|\mathbf{E}| = 1.02$ kV/cm. By rotating the dipoles, χ is varied continuously from negative to positive (Fig. 2g). At $\alpha = 0^\circ$, molecules interact repulsively as the dipole moments are aligned perpendicular to the 2D plane, leading to $\chi < 0$. At $\alpha = 90^\circ$, dipoles are aligned within the plane and the average interaction is attractive, leading to $\chi > 0$. Assuming symmetric transverse trapping, $\chi \propto -(3\cos^2\alpha - 1)$. Notably, this tunability of χ by rotating \mathbf{E} arises from a global geometric factor on the Ising and exchange interactions, in contrast to tuning with $|\mathbf{E}|$, which controls the relative strength of the two interactions.

The choice of the internal states used for the spin-1/2 system offers additional control over the interaction parameters. The green squares in Fig. 2e show a measurement of U_χ between $|\downarrow\rangle$ and $|\uparrow_2\rangle = |1, -1\rangle$ at $|\mathbf{E}| = 0$. Using $|\uparrow_2\rangle$ instead of $|\uparrow_1\rangle$ changes the magnitude of χ and reverses its sign at $|\mathbf{E}| = 0$, as a result of the different transition dipole moments in $\{|\downarrow\rangle, |\uparrow_2\rangle\}$ where $d_{\uparrow\downarrow} = -d_{\downarrow\uparrow} = \langle\downarrow|d|\uparrow_1\rangle/\sqrt{2}$. We measure χ between $|\downarrow\rangle$ and $|\uparrow_2\rangle$ to be $\chi_2 = 2.3(8)\times 10^{-6}$ Hz/cm², consistent with -1/2 of the interaction between $|\downarrow\rangle$ and $|\uparrow_1\rangle$ at this field.

The ability to manipulate dipolar interactions through the internal state allows us to dynamically change the interaction and the evolution of the many-body state. In contrast to tuning with the dc electric field, which can be limited by hyperfine state mixing or the electric field ramping speed, internal state control of the interaction can be achieved rapidly and coherently with microwave pulses. Such a capability is essential for applications such as dynamic Hamiltonian engineering³²

high fidelity quantum gate operations in molecular systems³³, and studying quantum quenched dynamics with dipolar spin systems^{34,35}.

By implementing a dynamical control pulse sequence, we demonstrate reversal of the coherent many-body spin dynamics. In particular, we coherently swap the excited state from $|\uparrow_2\rangle$ to $|\uparrow_1\rangle$ in the middle of the Ramsey evolution, which instantaneously changes the interaction parameter χ by a factor of -2, and consequently reverses the associated phase progress in a coherent evolution.

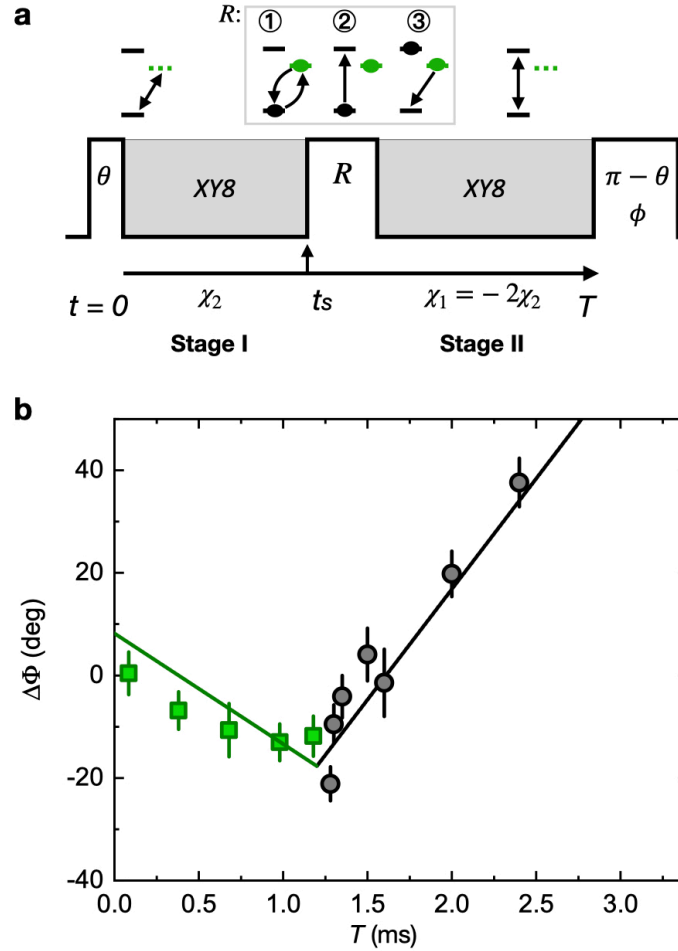


Figure 3. Reversal of the spin dynamics. **a.** Measurement sequence. Molecules are initially prepared and allowed to evolve in a superposition of $|\downarrow\rangle$ and $|\uparrow_2\rangle$. A composite pulse R coherently transfers the population in $|\uparrow_2\rangle$ to $|\uparrow_1\rangle$ while preserving its relative phase to $|\downarrow\rangle$. Molecules then evolve in $\{|\downarrow\rangle, |\uparrow_1\rangle\}$. Inset: Composition of R . **b.** Measured time evolution of $\Delta\Phi = \Delta\phi(\theta = \pi/4) - \Delta\phi(\theta = 3\pi/4)$ at $n = 1.1(1) \times 10^7 \text{ cm}^{-2}$. The phase accumulation in stage I (green squares) and stage II (black circles) are plotted over time. The total time plotted excludes the widths of the microwave pulses. A piecewise linear fit to the time evolution of $\Delta\Phi$ is shown as a solid line. The ratio between the two slopes is constrained to -2.

Our sequence consists of two phase accumulation stages, as illustrated in Fig. 3a. After a pulse with area θ prepares the molecules in a superposition of $|\downarrow\rangle, |\uparrow_2\rangle$, molecules evolve with χ_2 (stage I) until a composite microwave pulse R transfers the excited state population from $|\uparrow_2\rangle$ to $|\uparrow_1\rangle$. Molecules then continue to evolve in $\{|\downarrow\rangle, |\uparrow_1\rangle\}$ (stage II) with $\chi_1 = -2\chi_2$ before being detected after the final Ramsey pulse. The XY8 decoupling sequence is used during both stages. The composite pulse R consists of three consecutive Rabi- π pulses (Inset of Fig. 3a) in order to maintain the relative phase between the excited states and $|\downarrow\rangle$ during the state swapping. The duration of R is 70 μs , which is short compared to the interaction time scales.

We extract the phase shift $\Delta\Phi = \Delta\phi(\theta = \pi/4) - \Delta\phi(\theta = 3\pi/4)$ as a function of T (see Methods), plotted in Fig. 3b. For $T < 1.2$ ms, we fix the duration of stage II to be 80 μs and scan the time of stage I. For $T > 1.2$ ms, we fix the duration of stage I to be 1.2 ms and scan the time of stage II.

We observe a sign change in the rate of phase accumulation $d(\Delta\Phi)/dT$ at $t_s = 1.2$ ms when R is implemented, indicating a reversal of the mean-field interaction sign. The data is well described by a piecewise linear fit with the ratio of $d(\Delta\Phi)/dT$ before and after the reversal constrained to be -2 , consistent with the measurement in Fig. 2e. At $T \approx 1.6$ ms, $\Delta\Phi$ returns to the initial value, completing the phase reversal.

Our protocol realizes a *complete* reversal of the spin Hamiltonian at $|\mathbf{E}| = 0$. Such a capability is essential for studying out-of-time-ordered correlators which are used to understand dynamics of interacting quantum many-body systems such as quantum information scrambling³⁶⁻³⁹. Similar many-body echo processes also allow applications such as robust Heisenberg-limited phase sensitivity without single-particle-resolved state detection^{21,40-42}.

At long evolution times, motional and spin dynamics are coupled by the dipolar interaction, resulting in dynamical evolution beyond the spin model. Mode-changing dipolar collisions lead to loss of coherence, manifesting as an exponential decay of the Ramsey contrast, $\exp(-\Gamma t)$. Γ is proportional to the rate of elastic collisions $n\sigma v_T$, where v_T is the thermal velocity and σ is the cross section for dipolar elastic collisions. For spin-polarized fermionic molecules with dipole moment d induced by \mathbf{E} , previous theories^{43,44} and experiments^{15,17} have shown $\sigma \propto d^4$. By comparison, two molecules in a coherent superposition carry oscillating dipoles with amplitudes

of $d_{\downarrow\uparrow}$ in the lab frame, leading to dipolar collisions even at low $|\mathbf{E}|$ where induced dipole moments are small^{19,45}. When the oscillations are fully coherent, the molecules collide with maximum effective dipole moment $d_{\downarrow\uparrow}/\sqrt{2}$ and σ , with the $\sqrt{2}$ arising from time averaging of the oscillating dipole moments⁴⁵. These collisions couple the spin and motion, resulting in spin decoherence that cannot be removed using multi-pulse sequences, in contrast to interaction-induced dephasing in a lattice⁹.

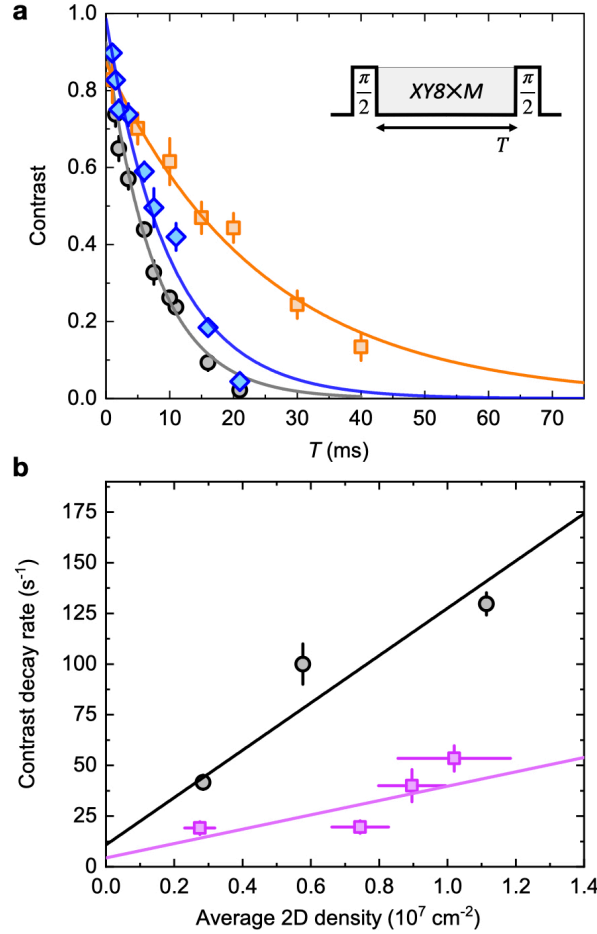


Figure 4. Dipolar collisional decoherence. **a.** Decay of Ramsey contrast between $|\downarrow\rangle$ and $|\uparrow_1\rangle$ for density $n = 1.1(1) \times 10^7 \text{ cm}^{-2}$ (grey circles), $0.57(4) \times 10^7 \text{ cm}^{-2}$ (blue diamonds), $0.28(3) \times 10^7 \text{ cm}^{-2}$ (orange squares) at $|\mathbf{E}| = 0$. Decoupling sequences used are XY8 \times 3 for the grey and blue traces and XY8 \times 7 for the orange trace. **b.** Contrast decay rate Γ as a function of n for $|\mathbf{E}| = 0$, $\alpha = 0^\circ$ (grey circles), and $|\mathbf{E}| = 1.02 \text{ kV/cm}$, $\alpha = 36^\circ$ (purple squares).

We study the effect of dipolar collisions by measuring the rate of contrast decay Γ as a function of n . To investigate collisional decoherence, the single particle dephasing rate must be below the collisional rate, which was achieved by increasing the number of decoupling pulses. We

experimentally found that XY8 \times 7 is sufficient for the lowest density measurements.

We observe the characteristic exponential decay of the contrast for a range of n , as shown in Fig. 4a for measurements at $|\mathbf{E}| = 0$. The extracted Γ increases with density (Fig. 4b), indicating that the coherence time is limited by collisions. At $n = 1.1(1) \times 10^7 \text{ cm}^{-2}$ and $|\mathbf{E}| = 0$, we measure $\Gamma = 130(5) \text{ s}^{-1}$, consistent with dipolar elastic collision rates measured in Ref. 15 with d being $d_{\downarrow\uparrow}/\sqrt{2}$ (see Methods). Rotating the electric field to $\alpha = 36^\circ$ at $|\mathbf{E}| = 1.02 \text{ kV/cm}$ reduces the strength of the dipolar interaction. We observe longer coherence times at the same density (purple squares in Fig. 4b), indicating reduced cross section for the dipolar elastic collisions.

By extracting the average $\sigma = \Gamma/nv_T$ for each electric field configuration, we found $\sigma(\alpha = 0^\circ, |\mathbf{E}| = 0)/\sigma(36^\circ, 1.02 \text{ kV/cm}) = 3.1(4)$. This variation of σ is expected to arise from the changing dipolar cross section as a function of α , similar to scattering with induced dipole moments^{17,44}. In analogy to the relationship in atomic systems between the mean-field shift ($\propto a$, where a is the s -wave scattering length) and elastic cross section ($\propto a^2$), the variation of σ could also be explained by a scaling $\sigma \propto \chi^2$. Our measured ratio of σ is consistent with $[\chi(0^\circ, 0)/\chi(36^\circ, 1.02 \text{ kV/cm})]^2 = 3.5(9)$, as measured in Fig. 2f, 2g. These results suggest that dipolar effects dominate the collisional decoherence process.

The high controllability of the dipolar quantum gas system allows tuning the motional dynamics relative to the coherent spin dynamics by changing parameters such as the strength of optical trapping⁴⁶, temperature via evaporation^{15,17,19}, and dipolar interaction strength. These capabilities would allow the investigation of other many-body spin-motion effects such as unconventional paired superfluidity^{47,48}, spin-wave and spin transport physics^{49,50}, and dipole-mediated spin-orbital dynamics⁵¹.

In conclusion, we have demonstrated tunable dynamics of the collective spin and motion in a 2D itinerant spin system formed from a gas of fermionic polar molecules. We have shown static and dynamical control over the spin Hamiltonian using external fields, microwaves, and internal states of the molecules. Our results establish a highly controllable spin system which can be used to investigate a broad range of many-body phenomena such as generation of highly entangled spin states, spin-orbital physics, or spin transport dynamics with molecules in 2D.

Methods

Molecular spin system and preparation

We create ultracold gases of KRb in 2D with the procedure detailed in Ref. 15 and Ref. 20. In brief, degenerate gases of ^{40}K and ^{87}Rb are loaded into a stack of 2D harmonic traps formed by a one-dimensional optical lattice. Molecules in the ground rotational state $|\downarrow\rangle$ are subsequently produced by magneto-association and stimulated Raman adiabatic passage (STIRAP) directly at \mathbf{E} . We typically produce 15×10^3 molecules at a temperature $T_0 \approx 450$ nK, occupying 19(1) layers with a peak number of about 1000 molecules in a single layer. The harmonic trapping frequencies within each layer for molecules in $|\downarrow\rangle$ at $|\mathbf{E}| = 0$ are $(\omega_x, \omega_y, \omega_z) = 2\pi \times (45, 17000, 45)$ Hz. Since the harmonic level spacing $\hbar\omega_y$ along the tight confinement direction is larger than $k_B T_0$ and the interaction energy scale, our molecules predominantly remain in the lowest harmonic level, forming a quasi-2D system throughout the experiments. Here, k_B is the Boltzmann constant. Couplings between these 2D layers are weak compared to the intralayer interaction²⁰, and we therefore approximate the system as a stack of isolated layers.

At $|\mathbf{E}| = 0$ and typical trapping condition, the resonant transition frequency between $|\downarrow\rangle$ and $|\uparrow_1\rangle$ ($|\downarrow\rangle$ and $|\uparrow_2\rangle$) is measured to be around 2228.138 MHz (2227.742 MHz). Compared to our typical Rabi frequency of 100 kHz, the large difference between resonant frequencies allows us to resolve these states by changing the microwave frequency.

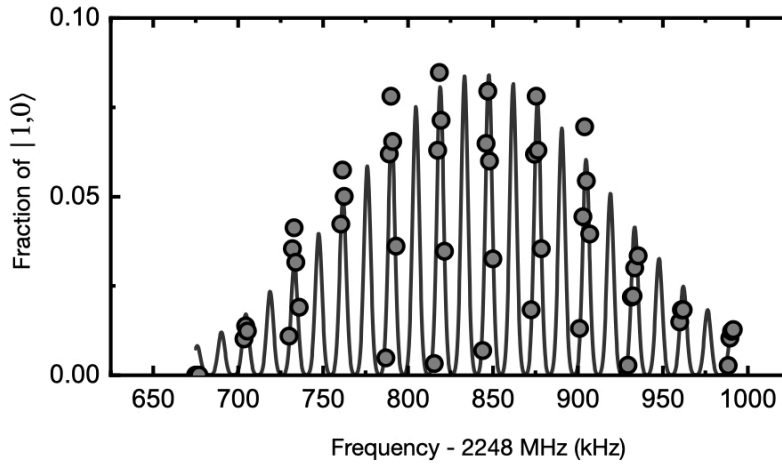
The density of the molecular gas is varied by adding an extra cleaning procedure after the molecules are produced and before the Ramsey interrogation. Specifically, a microwave pulse with an area of θ_c prepares molecules in a superposition of $|\downarrow\rangle$ and $|\uparrow_1\rangle$. The STIRAP beam that is resonant with $|\downarrow\rangle$ and the electronically-excited intermediate state of the molecules is switched on for 50 μs to eliminate the $|\downarrow\rangle$ component of the superposition. The remaining molecules are then flipped back to $|\downarrow\rangle$ with a π pulse. The density is reduced to $\sin^2(\theta_c/2)$ of the initial density. At certain values of \mathbf{E} , the cleaning STIRAP light pulse can also off-resonantly excite molecules in $|\uparrow_1\rangle$. In that case, molecules in $|\uparrow_1\rangle$ are shelved in $|2,0\rangle$ during the optical blast using an additional microwave pulse, and no loss of $|\uparrow_1\rangle$ molecules is observed.

Since the size of the STIRAP beam used for cleaning is larger than the size of the sample, we do not observe significant temperature change from the process. This method therefore allows us to

control the sample density without changing the temperature or the spatial distribution in the regime where the experiments are conducted.

2D density calibration

We use the following procedure to obtain the average 2D densities in the layers from the total molecule number N . The molecules occupy multiple layers formed by an optical lattice. We first measure the molecule distribution using layer-resolved spectroscopy²⁰. In brief, an electric field gradient along the longitudinal direction of the optical lattice shifts the transition frequency between $|0,0\rangle$ and $|1,0\rangle$ on each layer. When the differential shift for molecules in adjacent layers is large compared to the linewidth of the transition in each layer, molecules in different layers can be addressed, resolved, and measured spectroscopically using microwaves. A typical measurement (Extended data figure 1) reveals a Gaussian distribution with a full-width-half-maximum of 11(1) layers.



Extended data figure 1. A typical molecular number distribution measured via layer-resolved spectroscopy.

Grey circles are the experimental measurements. Black solid line is a fit to a summation of equally spaced Gaussian functions with a global Gaussian envelope. The width of each narrow Gaussian peak is assumed to be the same. The data is taken at $|E| = 1.02$ kV/cm and $\alpha = 36^\circ$ (magic condition) to reduce broadening of the single-layer transition linewidth due to differential polarizability.

For two-body processes considered in this work, such as the mean-field frequency shift and collisional decoherence, we calculate the average number of molecules per layer using an effective

number of layers L , defined as $L = \frac{N^2}{\sum_k N_k^2}$, where N_k is the number for molecules in the k -th layer.

From the layer-resolved number distribution, we extract $L = 19(1)$ and use $N_{2D} = N/L$ as the average number of molecules in a single layer. The average 2D density n is calculated from N_{2D} using temperatures measured with time-of-flight thermometry and the transverse trapping frequencies for $|\downarrow\rangle$ at E .

Our procedure for varying the density is not expected to change the number distribution across layers. We therefore use $L = 19$ for all our measurements.

Geometric factor of χ

The dipolar interaction between two dipoles has a geometric factor $(1-3\cos^2\Theta_{ij})$, where Θ_{ij} is the angle between the dipole moment and the vector between the two particles. When the molecular motion is confined to 2D, $\cos^2\Theta_{ij}$ can be decomposed into α and the azimuth angle β as $\cos^2\Theta_{ij} = \sin^2\alpha \cos^2\beta$. This geometric factor can be expressed in terms of α by taking the average over the harmonic oscillator states in the 2D plane. In the mean-field regime and with approximately symmetric transverse trapping, this averaging reduces to an average over β , yielding $\langle \cos^2\beta \rangle = 1/2$ and thus $\langle 1-3\cos^2\Theta_{ij} \rangle = (3\cos^2\alpha - 1)/2$.

Measurement of Ramsey coherence time

For the coherence time measurements, we measure the contrast at different Ramsey time T with the number of XY8 echo pulses fixed. To extract the contrast at each T , we perform 8 to 16 measurements of the fraction of $|\uparrow_1\rangle$ with ϕ equally spaced between 0 and 360 degrees. The contrast and its standard deviation (SD) at time T are extracted from the measured fractions via bootstrapping following the procedure described in Ref. 20.

Calibration of the decoupling pulse sequence

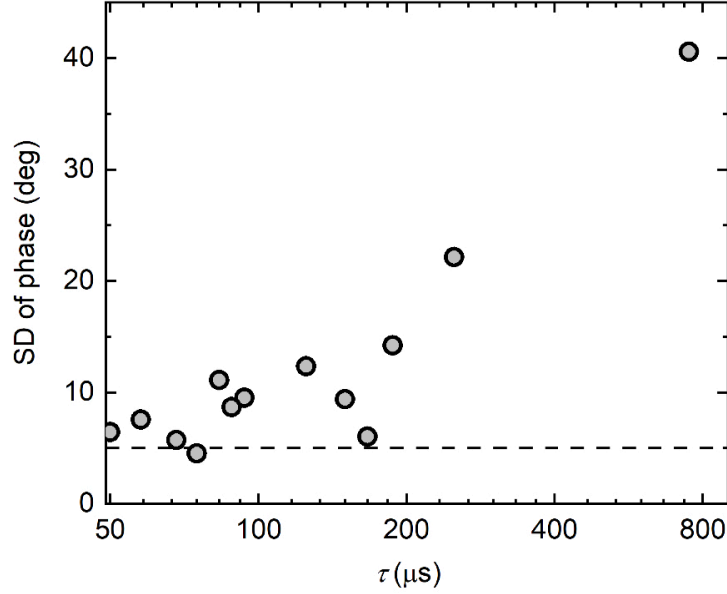
The XY8 sequence is designed to suppress fluctuations of the measured Ramsey phase due to fluctuating and irreproducible detunings caused by E , and the single particle dephasing. The efficacy of the suppression depends on the spacing τ between the Rabi- π pulses, pulse duration t_p , and the timing of the sequence, which we optimize with the following procedure:

An ideal XY8 sequence consists of infinitely fast echo pulses. However, if the microwave Rabi

frequency is too high, molecular hyperfine states that are not in the spin-1/2 manifold can be coupled off-resonantly by the microwave field. To avoid this effect, we limit the Rabi frequency such that the π pulses time is around 10 μs for measurements in $\{|\downarrow\rangle, |\uparrow_1\rangle\}$, and around 16 μs for measurements in $\{|\downarrow\rangle, |\uparrow_2\rangle\}$.

At fixed microwave power, we precisely determine the pulse duration in order to reduce the rotation error of the pulses. To do this, we perform a $\pi/2$ rotation followed immediately by up to 8 closely spaced echo pulses. We fine tune the pulse duration t_p until equal population of the two spin states are obtained regardless of the number of echo pulses applied.

The pulse spacing τ determines the passband frequency of the noise filter. Shorter τ gives higher passband frequencies and less sensitivity to low frequency electric field noise, which is the dominant noise source in our system. We characterize noise rejection as a function of τ by measuring the Ramsey phase fluctuations after a fixed T with $\{|\downarrow\rangle, |\uparrow_1\rangle\}$. We vary τ by changing the number of equally spaced Rabi- π pulses inserted between the two Ramsey pulses. We choose the phase of the second Ramsey pulse to maximize the sensitivity of the fraction of $|\uparrow_1\rangle$ to the Ramsey phase. For each τ , we repeat the measurement 10 times to extract the SD of Ramsey phase, as computed from the measured fraction of $|\uparrow_1\rangle$. We use echoes along \hat{X} only for this experiment, which provides the same electric field noise rejection performance as XY8.



Extended data figure 2. Noise suppression of the dynamical decoupling sequence. Data is taken at $|E| = 1.02$ kV/cm and $\alpha = 0^\circ$. We use X-echo only, which provides similar performance to XY8 in terms of rejecting noise in Δ . Each data point is extracted from 10 repetitions. The dashed line is the noise floor of our measurement.

Extended data figure 2 shows the SD of Ramsey phase as a function of τ for $T = 1.5$ ms. We observe reduction of the phase fluctuations as τ is reduced. To balance between decoupling efficacy and a high τ/t_p ratio to minimize system evolution during the pulses, we chose $\tau = 140 \mu\text{s}$ for the mean-field frequency shift measurements.

To account for the finite widths of the Ramsey pulses, we adjusted the delay ($\tau/2$ for infinitely short pulses) after the first Ramsey pulse and before the final detection pulse to minimize the sensitivity of the Ramsey phase shift to detuning Δ at resonance $(\partial\Delta\phi/\partial\Delta)_{\Delta=0}$ and maximize the range of Δ within which the phase shift is insensitive to Δ at first order. The amount of the adjustment is determined by simulating the XY8 sequence on a two-level system, and depends on the rotation angle θ , which is accounted for in the measurements.

Extracting phase shifts for the reversal measurements

Switching between two spin manifolds requires changing the frequency of the microwave source. We use two procedures to reduce extra phase shift introduced by this process: (1) we measure the

phase difference $\Delta\Phi = \Delta\phi(\theta = \pi/4) - \Delta\phi(\theta = 3\pi/4)$ between the Ramsey fringes obtained for $\theta = \pi/4$ and $\theta = 3\pi/4$; (2) For $\theta = 3\pi/4$ measurement, we first prepare the molecules in $|\uparrow_2\rangle$ instead of $|\downarrow\rangle$ and then apply a $\theta = \pi/4$ pulse. This allows us to keep the timings of the sequences for $\theta = \pi/4$ and $\theta = 3\pi/4$ identical.

Dipolar collisions with transition dipole moment

In Ref. 15, the dipolar elastic collision rate between spin polarized KRb in 2D was measured. With $n \approx 5.0 \times 10^7 \text{ cm}^{-2}$, $T_0 \approx 250 \text{ nK}$, $d = 0.2 \text{ D}$, Ref. 15 reported $\Gamma_0 = 168(48) \text{ s}^{-1}$. Scaling Γ_0 as $\Gamma \propto n \sqrt{T_0} d^4$ with $n = 1.1(1) \times 10^7 \text{ cm}^{-2}$, $T_0 = 463(9) \text{ nK}$, and $d = d_{\downarrow\uparrow}/\sqrt{2}$ (conditions for the grey circles in Fig. 4a), we obtain $\Gamma = 95(29) \text{ s}^{-1}$.

Acknowledgement

We thank Thomas Bilitewski and Ana Maria Rey for inspirational discussions and critical reading of the manuscript. We acknowledge funding from the DOE Quantum System Accelerator, the National Science Foundation QLCI OMA-2016244, the National Science Foundation Phys-1734006, and the National Institute of Standards and Technology. J. S. H. acknowledges support from the National Research Council postdoctoral fellowship.

Author contributions

All authors performed the experiments, analyzed the data, and contributed to interpreting the results and writing the manuscript.

Data availability

The datasets generated and analyzed during the current study are available from the corresponding authors on reasonable request.

Competing interests

The authors declare no competing interests.

References

1. Manousakis, E. The spin-1/2 Heisenberg antiferromagnet on a square lattice and its application to the cuprous oxides. *Rev. Mod. Phys.* **63**, 1–62 (1991).
2. Sobirey, L. *et al.* Observation of superfluidity in a strongly correlated two-dimensional Fermi gas. *Science* **372**, 844–846 (2021).
3. Wineland, D. J., Bollinger, J. J., Itano, W. M., Moore, F. L. & Heinzen, D. J. Spin squeezing and reduced quantum noise in spectroscopy. *Phys. Rev. A* **46**, R6797–R6800 (1992).
4. Nielsen, M. A. & Chuang, I. Quantum Computation and Quantum Information. *Am. J. Phys.* **70**, 558–559 (2002).
5. Bohn, J. L., Rey, A. M. & Ye, J. Cold molecules: Progress in quantum engineering of chemistry and quantum matter. *Science* **357**, 1002–1010 (2017).
6. Micheli, A., Brennen, G. K. & Zoller, P. A toolbox for lattice-spin models with polar molecules. *Nat. Phys.* **2**, 341–347 (2006).
7. Gorshkov, A. V *et al.* Quantum magnetism with polar alkali-metal dimers. *Phys. Rev. A* **84**, 033619 (2011).
8. Hazzard, K. R. A., Manmana, S. R., Foss-Feig, M. & Rey, A. M. Far-from-Equilibrium Quantum Magnetism with Ultracold Polar Molecules. *Phys. Rev. Lett.* **110**, 075301 (2013).
9. Yan, B. *et al.* Observation of dipolar spin-exchange interactions with lattice-confined polar molecules. *Nature* **501**, 521–525 (2013).
10. Barnett, R., Petrov, D., Lukin, M. & Demler, E. Quantum Magnetism with Multicomponent Dipolar Molecules in an Optical Lattice. *Phys. Rev. Lett.* **96**, 190401 (2006).
11. Christakis, L. *et al.* Probing site-resolved correlations in a spin system of ultracold molecules. *arXiv* (2022) doi:10.48550/ARXIV.2207.09328.
12. Kwasigroch, M. P. & Cooper, N. R. Bose-Einstein condensation and many-body localization of rotational excitations of polar molecules following a microwave pulse. *Phys. Rev. A* **90**, 021605 (2014).
13. Yao, N. Y., Zaletel, M. P., Stamper-Kurn, D. M. & Vishwanath, A. A quantum dipolar spin liquid. *Nat. Phys.* **14**, 405–410 (2018).

14. Mishra, T., Greschner, S. & Santos, L. Polar molecules in frustrated triangular ladders. *Phys. Rev. A* **91**, 043614 (2015).
15. Valtolina, G. *et al.* Dipolar evaporation of reactive molecules to below the Fermi temperature. *Nature* **588**, 239–243 (2020).
16. Matsuda, K. *et al.* Resonant collisional shielding of reactive molecules using electric fields. *Science* **370**, 1324–1327 (2020).
17. Li, J.-R. *et al.* Tuning of dipolar interactions and evaporative cooling in a three-dimensional molecular quantum gas. *Nat. Phys.* **17**, 1144–1148 (2021).
18. Anderegg, L. *et al.* Observation of microwave shielding of ultracold molecules. *Science* **373**, 779–782 (2021).
19. Schindewolf, A. *et al.* Evaporation of microwave-shielded polar molecules to quantum degeneracy. *Nature* **607**, 677–681 (2022).
20. Tobias, W. G. *et al.* Reactions between layer-resolved molecules mediated by dipolar spin exchange. *Science* **375**, 1299–1303 (2022).
21. Bilitewski, T. *et al.* Dynamical Generation of Spin Squeezing in Ultracold Dipolar Molecules. *Phys. Rev. Lett.* **126**, 113401 (2021).
22. Kitagawa, M. & Ueda, M. Squeezed spin states. *Phys. Rev. A* **47**, 5138–5143 (1993).
23. Leibfried, D. *et al.* Creation of a six-atom ‘Schrödinger cat’ state. *Nature* **438**, 639–642 (2005).
24. Neyenhuis, B. *et al.* Anisotropic Polarizability of Ultracold Polar $^{40}\text{K}^{87}\text{Rb}$ Molecules. *Phys. Rev. Lett.* **109**, 230403 (2012).
25. Seeßelberg, F. *et al.* Extending Rotational Coherence of Interacting Polar Molecules in a Spin-Decoupled Magic Trap. *Phys. Rev. Lett.* **121**, 253401 (2018).
26. Burchesky, S. *et al.* Rotational Coherence Times of Polar Molecules in Optical Tweezers. *Phys. Rev. Lett.* **127**, 123202 (2021).
27. Gullion, T., Baker, D. B. & Conradi, M. S. New, compensated Carr-Purcell sequences. *J. Magn. Reson.* **89**, 479–484 (1990).
28. Vandersypen, L. M. K. & Chuang, I. L. NMR techniques for quantum control and computation. *Rev. Mod. Phys.* **76**, 1037–1069 (2005).
29. Pham, L. M. *et al.* Enhanced solid-state multispin metrology using dynamical decoupling. *Phys. Rev. B* **86**, 45214 (2012).

30. Bishof, M., Zhang, X., Martin, M. J. & Ye, J. Optical Spectrum Analyzer with Quantum-Limited Noise Floor. *Phys. Rev. Lett.* **111**, 093604 (2013).
31. Souza, A. M., Álvarez, G. A. & Suter, D. Effects of time-reversal symmetry in dynamical decoupling. *Phys. Rev. A* **85**, 032306 (2012).
32. Geier, S. *et al.* Floquet Hamiltonian engineering of an isolated many-body spin system. *Science* **374**, 1149–1152 (2021).
33. Ni, K.-K., Rosenband, T. & Grimes, D. D. Dipolar exchange quantum logic gate with polar molecules. *Chem. Sci.* **9**, 6830–6838 (2018).
34. Eisert, J., Friesdorf, M. & Gogolin, C. Quantum many-body systems out of equilibrium. *Nat. Phys.* **11**, 124–130 (2015).
35. Guardado-Sanchez, E. *et al.* Probing the Quench Dynamics of Antiferromagnetic Correlations in a 2D Quantum Ising Spin System. *Phys. Rev. X* **8**, 021069 (2018).
36. Shenker, S. H. & Stanford, D. Black holes and the butterfly effect. *J. High Energy Phys.* **2014**, 67 (2014).
37. Maldacena, J., Shenker, S. H. & Stanford, D. A bound on chaos. *J. High Energy Phys.* **2016**, 106 (2016).
38. Braumüller, J. *et al.* Probing quantum information propagation with out-of-time-ordered correlators. *Nat. Phys.* **18**, 172–178 (2022).
39. Green, A. M. *et al.* Experimental Measurement of Out-of-Time-Ordered Correlators at Finite Temperature. *Phys. Rev. Lett.* **128**, 140601 (2022).
40. Davis, E., Bentsen, G. & Schleier-Smith, M. Approaching the Heisenberg Limit without Single-Particle Detection. *Phys. Rev. Lett.* **116**, 053601 (2016).
41. Colombo, S. *et al.* Time-Reversal-Based Quantum Metrology with Many-Body Entangled States. (2021) doi:10.48550/ARXIV.2106.03754.
42. Gilmore, K. A. *et al.* Quantum-enhanced sensing of displacements and electric fields with two-dimensional trapped-ion crystals. *Science* **373**, 673–678 (2021).
43. Bohn, J. L., Cavagnero, M. & Ticknor, C. Quasi-universal dipolar scattering in cold and ultracold gases. *New J. Phys.* **11**, 55039 (2009).
44. Ticknor, C. Quasi-two-dimensional dipolar scattering. *Phys. Rev. A* **81**, 042708 (2010).
45. Karman, T., Yan, Z. Z. & Zwierlein, M. Resonant and first-order dipolar interactions between ultracold $^1\Sigma$ molecules in static and microwave electric fields. *Phys. Rev. A* **105**,

- 013321 (2022).
46. Martin, M. J. *et al.* A Quantum Many-Body Spin System in an Optical Lattice Clock. *Science* **341**, 632–636 (2013).
 47. Bruun, G. M. & Taylor, E. Quantum Phases of a Two-Dimensional Dipolar Fermi Gas. *Phys. Rev. Lett.* **101**, 245301 (2008).
 48. Lee, H., Matveenko, S. I., Wang, D.-W. & Shlyapnikov, G. V. Fulde-Ferrell-Larkin-Ovchinnikov state in bilayer dipolar systems. *Phys. Rev. A* **96**, 061602 (2017).
 49. Peter, D., Müller, S., Wessel, S. & Büchler, H. P. Anomalous Behavior of Spin Systems with Dipolar Interactions. *Phys. Rev. Lett.* **109**, 025303 (2012).
 50. Koschorreck, M., Pertot, D., Vogt, E. & Köhl, M. Universal spin dynamics in two-dimensional Fermi gases. *Nat. Phys.* **9**, 405–409 (2013).
 51. Syzranov, S. V., Wall, M. L., Gurarie, V. & Rey, A. M. Spin–orbital dynamics in a system of polar molecules. *Nat. Commun.* **5**, 5391 (2014).